

Reduced-magnetohydrodynamic simulations of toroidally and poloidally localized edge localized modes

M. Hölzl, S. Günter, R. P. Wenninger, W.-C. Müller, G. T. A. Huysmans et al.

Citation: *Phys. Plasmas* **19**, 082505 (2012); doi: 10.1063/1.4742994

View online: <http://dx.doi.org/10.1063/1.4742994>

View Table of Contents: <http://pop.aip.org/resource/1/PHPAEN/v19/i8>

Published by the [American Institute of Physics](#).

Related Articles

Two-dimensional plasma expansion in a magnetic nozzle: Separation due to electron inertia

Phys. Plasmas **19**, 083501 (2012)

Plasma relaxation and topological aspects in Hall magnetohydrodynamics

Phys. Plasmas **19**, 072124 (2012)

Supersonic regime of the Hall-magnetohydrodynamics resistive tearing instability

Phys. Plasmas **19**, 072519 (2012)

Role of ion mass in the generation of fluctuations and poloidal flows in a simple toroidal plasma

Phys. Plasmas **19**, 072306 (2012)

Influence of magnetic field strength on potential well in the ionization stage of a double stage Hall thruster

Phys. Plasmas **19**, 073511 (2012)

Additional information on Phys. Plasmas

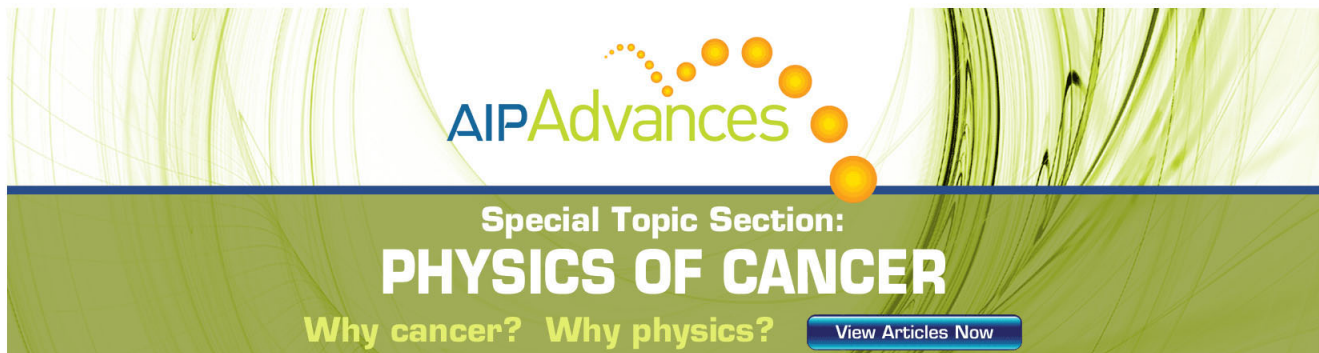
Journal Homepage: <http://pop.aip.org/>

Journal Information: http://pop.aip.org/about/about_the_journal

Top downloads: http://pop.aip.org/features/most_downloaded

Information for Authors: <http://pop.aip.org/authors>

ADVERTISEMENT



AIP Advances

Special Topic Section:
PHYSICS OF CANCER

Why cancer? Why physics? [View Articles Now](#)

Reduced-magnetohydrodynamic simulations of toroidally and poloidally localized edge localized modes

M. Hölzl,¹ S. Günter,¹ R. P. Wenninger,² W.-C. Müller,¹ G. T. A. Huysmans,³ K. Lackner,¹ I. Krebs,¹ and ASDEX Upgrade Team

¹Max-Planck-Institut für Plasmaphysik, EURATOM Association, Boltzmannstraße 2, 85748 Garching, Germany

²Universitätssternwarte der Ludwig-Maximilians-Universität, 81679 München, Germany

³ITER Organisation, Route de Vinon sur Verdon, St-Paul-lez-Durance, France

(Received 27 January 2012; accepted 16 July 2012; published online 7 August 2012)

We use the non-linear reduced-magnetohydrodynamic code JOREK to study edge localized modes (ELMs) in the geometry of the ASDEX Upgrade tokamak. Toroidal mode numbers, poloidal filament sizes, and radial propagation speeds of filaments into the scrape-off layer are in good agreement with observations for type-I ELMs in ASDEX Upgrade. The observed instabilities exhibit a toroidal and poloidal localization of perturbations which is compatible with the “solitary magnetic perturbations” recently discovered in ASDEX Upgrade [R. Wenninger *et al.*, “Solitary magnetic perturbations at the ELM onset,” Nucl. Fusion (accepted)]. This localization can only be described in numerical simulations with high toroidal resolution. [<http://dx.doi.org/10.1063/1.4742994>]

I. INTRODUCTION

Edge localized modes (ELMs) accompany the high-confinement mode (H-mode) in tokamak fusion plasmas. As they could cause a potentially destructive heat-load on divertor plates and wall structures in large fusion devices,^{1,2} detailed understanding of these instabilities and of mitigation-techniques is important for a successful operation of ITER. Non-linear magnetohydrodynamic (MHD) simulations with the JOREK code,^{3–9} which is also used for the present article, and other codes like BOUT++,¹⁰ NIMROD,¹¹ or M3D¹² can make an important contribution after successful benchmarks with measurements in existing tokamaks.

In the present article, a comparison between simulations with the non-linear finite-element code JOREK¹³ and observations in the ASDEX Upgrade tokamak¹⁴ is started. We concentrate on the early phase of ELMs. JOREK solves the reduced MHD equations in realistic X-point geometries as described in Sec. II. ASDEX Upgrade is equipped with a unique set of edge diagnostics that allows to investigate ELM crashes with high spatial and temporal resolutions.¹⁵ This provides excellent possibilities for theory-experiment comparisons. Emphasis is put on simulations with high toroidal resolution (many toroidal modes at toroidal periodicity 1) to treat the coupling between various toroidal modes properly. This way, aspects can be identified that are described well already at low toroidal resolution (few toroidal modes at a high toroidal periodicity) while others are influenced significantly by the non-linear toroidal mode-coupling.

The article is structured as follows. Section II describes the non-linear MHD-code JOREK. Physical parameters and technical details of the numerical simulations are given in Sec. III. Our observations and findings made in the simulated instabilities are presented in Sec. IV. Subsequently, Sec. V describes how these results compare to experimental

measurements. Finally, Sec. VI summarizes and gives a brief outlook.

II. JOREK CODE

The simulations are carried out with the single-fluid reduced-MHD model of the JOREK code. Section II A describes the equations solved in this model. For more details on the derivation, refer Ref. 16 and the Appendix. Spatial and temporal discretizations are briefly addressed in Sec. II B.

A. Reduced-MHD equations

Seven physical variables are treated: poloidal flux Ψ , stream function u , toroidal current density j , toroidal vorticity ω , density ρ , temperature T , and velocity v_{\parallel} along magnetic field lines. The normalization of the relevant quantities is listed in Table I.

Variables j and ω are connected to Ψ and u by the definition equations

$$j = \Delta^* \Psi = R^2 \nabla_{pol} \cdot (R^{-2} \nabla_{pol} \Psi) = R \frac{d}{dR} \left(\frac{1}{R} \frac{d\Psi}{dR} \right) + \frac{d^2 \Psi}{dZ^2}, \quad (1)$$

$$\omega = \nabla_{pol}^2 u = \frac{1}{R} \frac{d}{dR} \left(R \frac{du}{dR} \right) + \frac{d^2 u}{dZ^2}, \quad (2)$$

where ∇_{pol} denotes the del-operator in the poloidal plane, R the major radius, and Z the vertical coordinate. The time-evolution of the remaining five free variables is described by the following set of equations (called physics-model “302” in JOREK):

$$\frac{\partial \Psi}{\partial t} = \eta j - R[u, \Psi] - F_0 \frac{\partial u}{\partial \phi}, \quad (3)$$

TABLE I. The normalization of quantities in JOEAK is listed. It corresponds to choosing scale factors $B_0 = 1\text{T}$ and $R_0 = 1\text{m}$. Variable names with subscript ‘‘SI’’ denote quantities in SI units, while variables without this subscript are the ones used in JOEAK. In the presented simulations, $n_0 = 6 \cdot 10^{19}\text{m}^{-3}$ and $\rho_0 = 2 \cdot 10^{-7}\text{kgm}^{-3}$. The magnetic constant is denoted μ_0 and the Boltzmann constant k_B .

R_{SI} [m]	$= R$	Major radius
Z_{SI} [m]	$= Z$	Vertical coordinate
\mathbf{B}_{SI} [T]	$= \mathbf{B}$	Magnetic field vector; see Eq. (9)
Ψ_{SI} [Tm ²]	$= \Psi$	Poloidal magnetic flux
$j_{\phi,\text{SI}}$ [Am ⁻²]	$= -j/(R\mu_0)$	Toroidal current density; $j_{\phi,\text{SI}} = \mathbf{j}_{\text{SI}} \cdot \hat{\mathbf{e}}_{\phi}$
n_{SI} [m ⁻³]	$= \rho n_0$	Particle density
ρ_{SI} [kgm ⁻³]	$= \rho \rho_0$	Mass density = ion mass \times particle density
T_{SI} [K]	$= T/(k_B \mu_0 n_0)$	Temperature = electron + ion temperature
p_{SI} [Nm ⁻²]	$= \rho T/\mu_0$	Plasma pressure
\mathbf{v}_{SI} [ms ⁻¹]	$= \mathbf{v}/\sqrt{\mu_0 \rho_0}$	Velocity vector; see Eq. (8)
$v_{\parallel,\text{SI}}$ [ms ⁻¹]	$= v_{\parallel} \cdot \mathbf{B}_{\text{SI}}/\sqrt{\mu_0 \rho_0}$	Parallel velocity component, where $B_{\text{SI}} = \mathbf{B}_{\text{SI}} $
u_{SI} [ms ⁻¹]	$= u/\sqrt{\mu_0 \rho_0}$	Velocity stream function
$\omega_{\phi,\text{SI}}$ [m ⁻¹ s ⁻¹]	$= \omega/\sqrt{\mu_0 \rho_0}$	Toroidal vorticity; see Eq. (2)
t_{SI} [s]	$= t \cdot \sqrt{\mu_0 \rho_0}$	Time
γ_{SI} [s ⁻¹]	$= \gamma/\sqrt{\mu_0 \rho_0}$	Growth rate; $\gamma_{\text{SI}} = \ln[E_{\text{SI}}(t_2)/E_{\text{SI}}(t_1)]/[2\Delta t_{\text{SI}}]$; Energy $E_{\text{SI}}[\text{J}]$
η_{SI} [Ωm]	$= \eta \cdot \sqrt{\mu_0/\rho_0}$	Resistivity
ν_{SI} [kgm ⁻¹ s ⁻¹]	$= \nu \cdot \sqrt{\rho_0/\mu_0}$	Dynamic viscosity
D_{SI} [m ² s ⁻¹]	$= D/\sqrt{\mu_0 \rho_0}$	Particle diffusivity (\parallel or \perp)
K_{SI} [m ⁻¹ s ⁻¹]	$= K \cdot n_0/\sqrt{\mu_0 \rho_0}$	Heat diffusivity (\parallel or \perp), where $\chi_{\text{SI}} [\text{m}^2\text{s}^{-1}] = K_{\text{SI}}/n_{\text{SI}}$
$S_{T,\text{SI}}$ [Wm ⁻³]	$= S_T/\sqrt{\mu_0^3 \rho_0}$	Heat source
$S_{\rho,\text{SI}}$ [kgs ⁻¹ m ⁻³]	$= S_{\rho} \cdot \sqrt{\rho_0/\mu_0}$	Particle source

$$\frac{\partial \rho}{\partial t} = -\nabla \cdot (\rho \mathbf{v}) + \nabla \cdot (D_{\perp} \nabla_{\perp} \rho) + S_{\rho}, \quad (4)$$

$$\rho \frac{\partial T}{\partial t} = -\rho \mathbf{v} \cdot \nabla T - (\kappa - 1) p \nabla \cdot \mathbf{v} + \nabla \cdot (K_{\perp} \nabla_{\perp} T + K_{\parallel} \nabla_{\parallel} T) + S_T, \quad (5)$$

$$\hat{\mathbf{e}}_{\phi} \cdot \nabla \times \left\{ \rho \frac{\partial \mathbf{v}}{\partial t} = -\rho (\mathbf{v} \cdot \nabla) \mathbf{v} - \nabla p + \mathbf{j} \times \mathbf{B} + \nu \Delta \mathbf{v} \right\}, \quad (6)$$

$$\mathbf{B} \cdot \left\{ \rho \frac{\partial \mathbf{v}}{\partial t} = -\rho (\mathbf{v} \cdot \nabla) \mathbf{v} - \nabla p + \mathbf{j} \times \mathbf{B} + \nu \Delta \mathbf{v} \right\}. \quad (7)$$

In every time-step, Eqs. (1)–(7) are solved simultaneously in weak form as a large sparse implicit system of equations. The velocity vector is defined as

$$\mathbf{v} = -R \nabla u \times \hat{\mathbf{e}}_{\phi} + v_{\parallel} \mathbf{B}, \quad (8)$$

the magnetic field vector as

$$\mathbf{B} = (F_0 \hat{\mathbf{e}}_{\phi} + \nabla \Psi \times \hat{\mathbf{e}}_{\phi})/R, \quad (9)$$

the pressure is $p = \rho T$, and $\kappa = 5/3$ denotes the ratio of specific heats. Here, $\hat{\mathbf{e}}_{\phi}$ denotes the normalized toroidal basis vector. The toroidal magnetic field $B_{\phi} = F_0/R$ is fixed and cannot change with time. The poloidal velocity, i.e., the velocity vector in the poloidal plane, is denoted \mathbf{v}_{pol} . The parallel gradient is given by $\nabla_{\parallel} = \mathbf{b} \cdot \nabla$, where $\mathbf{b} = \mathbf{B}/|\mathbf{B}|$, and the perpendicular gradient by $\nabla_{\perp} = \nabla - \nabla_{\parallel}$. The Poisson bracket $[u, \Psi]$ is defined as $\frac{\partial u}{\partial R} \frac{\partial \Psi}{\partial Z} - \frac{\partial u}{\partial Z} \frac{\partial \Psi}{\partial R}$. Note, that the

poloidal components of the velocity in this set of equations are determined only by the $\mathbf{E} \times \mathbf{B}$ -drift term. As a result, u acts as a velocity stream function and (except for a factor F_0) also as electric potential.

Ideal-wall boundary conditions are implemented where the boundary of the computational domain is parallel to the magnetic flux surfaces. At the divertor targets, where the flux surfaces intersect the computational boundary, modified Bohm boundary conditions apply.^{4,17}

B. Discretization

The poloidal plane is discretized by 2D Bezier finite elements with four degrees of freedom per grid node and physical variable,¹³ while a Fourier decomposition is applied toroidally. The number of toroidal modes resolved in the simulations and the assumed toroidal periodicity of the system can be chosen separately. A periodicity equal to one means that the solution is computed for the whole torus. For larger periodicities, only a toroidal section of the torus is resolved. The modes included in the presented simulations are listed in Table II.

The temporal discretization is performed by a fully implicit second-order linearized Crank-Nicholson scheme.¹⁸ In the resulting large sparse system, all physical equations and all toroidal harmonics are coupled. It is solved by an iterative generalized minimal residual (GMRES) method, where a physics-based preconditioning is applied at the beginning of each GMRES solver step. In the preconditioning, the coupling between the sub-matrices corresponding to individual toroidal harmonics is neglected which allows to solve each

TABLE II. The toroidal mode numbers resolved in simulations with different periodicities are listed.

Periodicity	Resolved n -modes
8	0,8,16
4	0,4,8,12,16
2	0,2,4,...,12,14,16
1	0,1,2,...,14,15,16

sub-system separately. This is performed using the direct solver PaStiX.¹⁹

III. SIMULATIONS

Simulations of edge-localized modes are one of the most challenging tasks in fusion MHD numerics. The problem must be treated in realistic X-point geometry as the mode-affected region extends from inside the H-mode pedestal into the scrape-off layer, the vacuum region, and to the divertor legs. High spatial resolutions in all dimensions are required due to the small scales of the structures and the large radial gradients of equilibrium quantities at the pedestal. Thus, as a consequence of limited computational resources, not all aspects of an experiment can be described realistically in simulations so far. For instance, simulations with high resolution in radial and poloidal directions, i.e., with a large number of 2D Bezier finite-elements in the case of JOREK, render important investigations at more realistic plasma resistivities possible (e.g., Ref. 8), but only at a very limited number of toroidal Fourier harmonics.

For this work, a different choice was made: The focus is put on high toroidal resolution. This is done to investigate the influence of toroidal mode-coupling onto the non-linear evolution of an ELM. The mode numbers resolved in the simulations are listed in Table II. All runs resolve the $n = 0, \dots, 16$ range but with different periodicities. The relatively high number of toroidal modes involved limits the possible radial and poloidal resolutions: Most simulations are carried out with about 5500 Bezier elements. The corresponding finite-element grid is shown in Figure 1. Only for the simulations with lower plasma resistivity (denoted “eta6” runs, see the next paragraph for details), the number of Bezier elements is increased by a factor of two. Grid accumulation is used to increase the resolution radially around the separatrix and poloidally around the X-point.

Due to the comparably low poloidal resolution, only plasma resistivities significantly larger than in the experiment can be resolved. The respective simulation parameters are listed in Table III. The limited poloidal resolution also reduces the growth rate of modes with high mode numbers artificially. Thus when increasing the poloidal resolution, the most unstable mode number would shift towards larger n . On the other hand, diamagnetic stabilization is not taken into account in the simulations. Including this effect would have a stabilizing effect onto high poloidal mode numbers. The electron diamagnetic frequency for $n = 10$ is about 10^5 s^{-1} (calculated at a normalized poloidal flux of $\Psi_N = 0.9$). This is comparable to the fastest linear growth rates in the

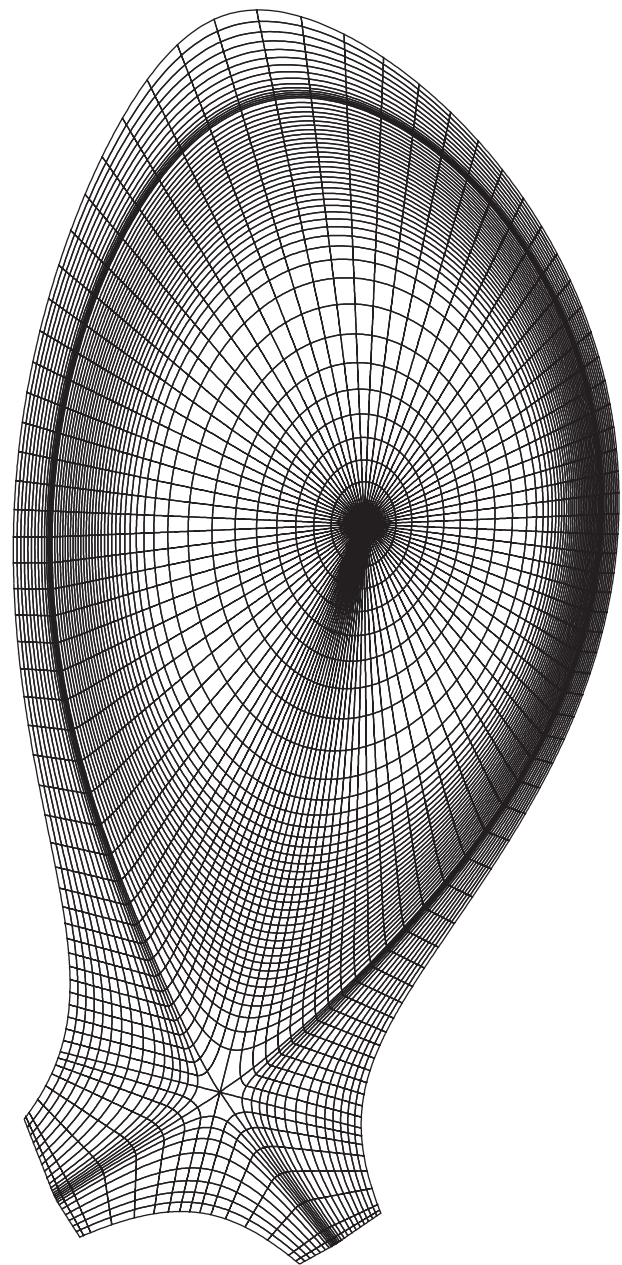


FIG. 1. The flux-surface aligned X-point grid with 5500 Bezier finite-elements is shown. The number of grid points are 96 poloidal points, 40 radial points inside the separatrix, 15 radial points outside the separatrix, 9 “radial” points in the private flux region, and 9 grid points along the divertor legs. For the eta6 simulations, these numbers are all increased by a factor of $\sqrt{2}$, leading to about 11000 Bezier elements.

simulations (see Sec. IV). Thus, the most unstable mode numbers would probably be similar in simulations with higher poloidal resolution and diamagnetic stabilization taken into account.

All simulations are based on typical ASDEX Upgrade discharge parameters—the details are given in Sec. III A. The simulations concentrate on the early phase of an ELM-crash up to the point where filaments start to form. The computations are carried out mostly on the HPC-FF cluster located in Jülich, Germany. The eta5 simulations with periodicity 1 and about 5500 Bezier elements require at least 102 compute nodes (8 cores and 24 GB of memory each) due to memory requirements of the solver and take about ten

TABLE III. Core values for plasma resistivity and viscosity are listed for the simulations denoted eta5 and eta6. Both quantities are modelled with a $T^{-3/2}$ dependence and are chosen significantly larger than in experiments due to computational restrictions. In ASDEX Upgrade, the core resistivity is typically about $10^{-8} \Omega\text{m}$.

Run	$\eta_{\text{SI}} [\Omega\text{m}]$	$\nu_{\text{SI}} [\text{m}^2/\text{s}]$
eta5	5×10^{-5}	7.5×10^{-5}
eta6	5×10^{-6}	7.5×10^{-6}

thousand CPU hours to complete. The eta6 computation with 11000 Bezier elements is at the limit of what can be investigated with JOEAK on this machine.

A. Physical parameters

A typical ASDEX Upgrade H-mode discharge with type-I ELMs constitutes the basis of the simulations: Geometry and profiles are taken from discharge 23221 at 4.7 s with a plasma current of 1 MA, 8 MW of neutral beam injection heating, and 1.5 MW of electron cyclotron resonance heating. The equilibrium reconstruction with the CLISTE code^{20,21} takes into account measured kinetic profiles. Source terms S_ρ and S_T and perpendicular diffusivities D_\perp and K_\perp are adjusted such that the equilibrium does not change significantly with time. The core temperature is $k_B T_{\text{SI}} = k_B (T_{e,\text{SI}} + T_{i,\text{SI}}) = 12.4 \text{ keV}$. The safety-factor takes a value of $q(0) = 1$ in the plasma core and $q(\Psi_N = 0.95) = 4.7$ close to the separatrix, where $\Psi_N = (\Psi - \Psi_{\text{axis}}) / (\Psi_{\text{separatrix}} - \Psi_{\text{axis}})$ denotes the normalized poloidal flux. A pure deuterium plasma with a core density of $6 \cdot 10^{19} \text{ m}^{-3}$ is assumed. The heat diffusion anisotropy, K_{\parallel}/K_\perp , takes a value of $7 \cdot 10^6$ at the separatrix.

The spatial resolution required for the simulation is, amongst others, determined by the resistive skin depth $\delta_{\text{SI}} = \sqrt{2\eta_{\text{SI}}/(\mu_0\gamma_{\text{SI}})}$ which is about 6 mm in eta6 simulations. As the spatial resolution possible in the poloidal plane is limited by computational resources, realistic plasma resistivities with a resistive skin depth of about 0.3 mm cannot be resolved (resolving spatial scales smaller than the ion gyro-radius is of course not reasonable anyway in MHD-simulations).

The following data are used as inputs for the JOEAK simulation:

- From experimental measurements: Temperature and density profiles, and toroidal magnetic field strength. The pressure profile is shown in Figure 2(a).
- From CLISTE-equilibrium reconstruction based on experimental measurements: FF' -profile and the values of the poloidal flux Ψ at the JOEAK computational boundary. Here, $F = (2\pi/\mu_0) J_{\text{pol,SI}}$ is proportional to the poloidal plasma current, J_{pol} , and $F' = dF/d\Psi$. The q -profile of the equilibrium is shown in Figure 2(b).

In JOEAK simulations, the Grad-Shafranov equation is solved first based on these input parameters. The equilibrium perfectly agrees with CLISTE (q -profile, flux surfaces, etc.). After that, an ‘‘equilibrium refinement’’ phase is required where the time-evolution equations are solved

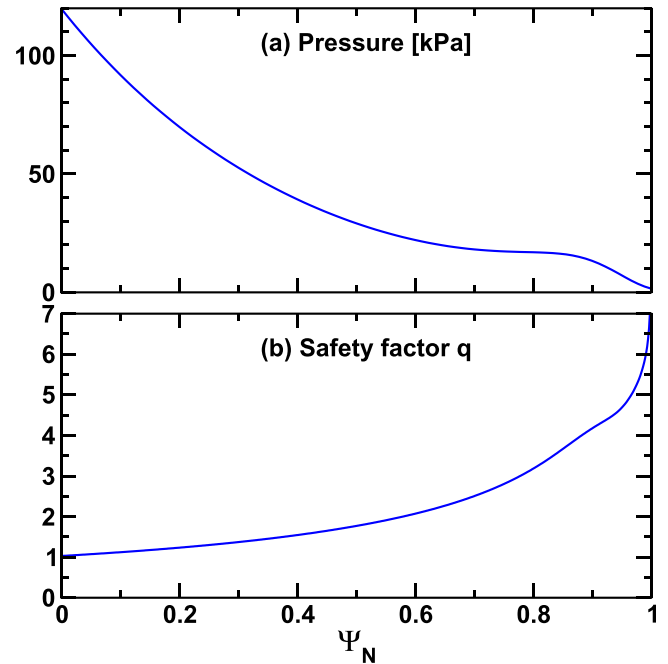


FIG. 2. Profiles of (a) plasma pressure and (b) safety-factor are shown for the plasma equilibrium used in the simulations.

only for the $n = 0$ mode, with very small time-steps that are gradually increased. This allows plasma flows to equilibrate.⁶ Successively, the reduced MHD equations are evolved in time, taking into account some or many toroidal Fourier modes depending on the case considered. Instabilities then develop out of an initially very small random perturbation.

IV. SIMULATION RESULTS

In the following, the simulation results are described and analyzed. Section IV A addresses simulations with low toroidal resolution, while Sec. IV B covers the situation at high toroidal resolution. In the succeeding Sec. IV C, an attempt towards more realistic plasma resistivities is made. The simulation results are compared to experimental findings in Sec. V.

A. Low toroidal resolution

This section provides simulation results for periodicity 8, where only the toroidal modes $n = 0, 8,$ and 16 are resolved. A ballooning-like exponentially growing mode located close to the plasma boundary develops at the low-field side. As seen in the energy diagnostics shown in Figure 3, the $n = 8$ mode is linearly more unstable (growth rate $\gamma_{\text{SI}} = 2.0 \times 10^5 \text{ s}^{-1}$) than the $n = 16$ mode ($\gamma_{\text{SI}} \approx 1.5 \times 10^5 \text{ s}^{-1}$). Due to mode-coupling, the structure of the $n = 16$ mode changes at $t = 284 \mu\text{s}$ in the simulation—the position of its maximum amplitude moves radially from the $q = 4$ to the adjacent $q = 3.75$ resonant surface. Hereby, the growth rate of the $n = 16$ mode increases significantly to $\gamma_{\text{SI}} = 4.3 \times 10^5 \text{ s}^{-1}$ which is roughly the double $n = 8$ growth rate. The $n = 8$ mode also remains dominant at the onset of non-linear mode saturation ($t \approx 300 \mu\text{s}$).

The ballooning-structure that develops at the whole low-field side of the plasma is shown in Figure 4 for time point

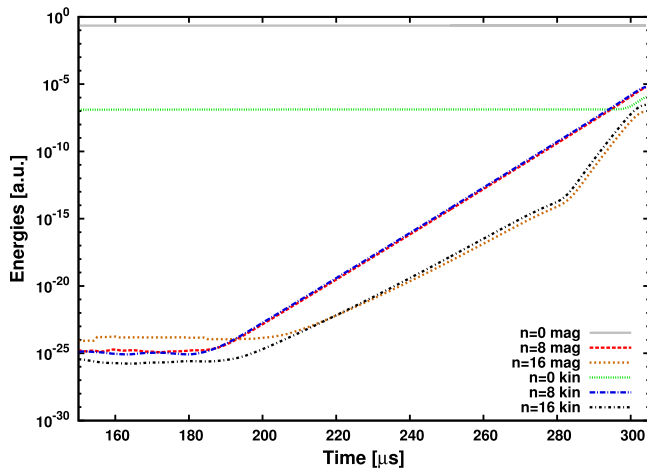


FIG. 3. Time-traces of the magnetic and kinetic energies contained in the individual toroidal harmonics are plotted for the simulation with periodicity 8. The $n = 8$ mode is linearly more unstable than the $n = 16$ mode and also remains dominant when non-linear saturation sets in. Due to non-linear mode-interaction, the growth rate of the $n = 16$ mode increases significantly at $t = 284 \mu\text{s}$. The $n = 0$ magnetic energy is dominated by the toroidal magnetic field which is fixed in time as described in Sec. IV A.

298 μs in the simulation. The “density-fingers” are very regular with a poloidal size of about 15–20 cm at the outer midplane. The poloidal “compression” of the structures in the vicinity of the lower (active) and the upper (inactive) X-points compared to the outer midplane is a consequence of field-line stagnation; the poloidal width of the structures is roughly constant in the straight-fieldline angle θ^* . In

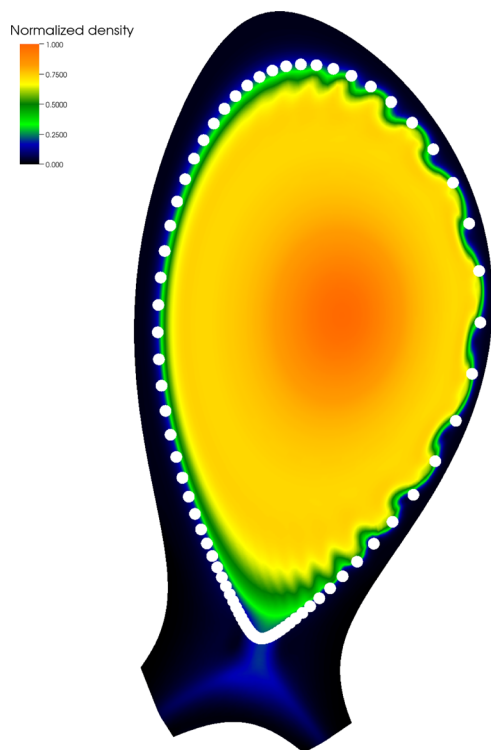


FIG. 4. The density distribution with developing ballooning-structure in the simulation with periodicity 8 is shown at 298 μs . Regular ballooning-structures are observed on the whole low-field side. All ballooning-fingers are roughly equally wide in poloidal direction in the straight-fieldline angle θ^* (the white dots indicate equidistant distances in θ^*).

Figure 4, this can be seen by comparing the density fingers to the white dots which divide the poloidal circumference into equidistant sections in θ^* . When the exponentially growing perturbation gets visible in the density distribution, distortions start to build up which propagate into the vacuum region as finger-like structures with significantly increased density due to the $E \times B$ drift. Their radial velocity, measured by tracing the position at which the density equals 10 percent of the core density, increases to about 3 km/s and saturates at that level. In the beginning, the density shows sinusoidal excursions of the density contours which grow over time (linear phase). As the instability grows and non-linear saturation sets in (energy growth rates start to decrease), the density fingers develop sub-structures. The changing structure also reflects in a different mode-spectrum, where the $n = 16$ energies get closer to the $n = 8$ energies (Figure 3). The ideal-wall boundary conditions contribute to the saturation of radial velocity when the distance between the mode and the wall gets significantly smaller than its poloidal wave-length as mirror-currents build up that slow down the mode-evolution.

B. High toroidal resolution

Now, the same setup as in the previous Section is considered at periodicity 1: All toroidal modes in the range $n = 0$ to 16 are resolved. The comparison of simulations with different periodicities allows to identify effects caused by the coupling between toroidal modes.

Time-traces of the magnetic energies contained in each toroidal harmonic are shown in Figure 5. Linearly, the $n = 10$ mode has the largest growth rate $\gamma_{\text{SI}} \approx 2.0 \times 10^5 \text{ s}^{-1}$. In a similar way as described for the $n = 16$ mode in Sec. IV A, the initially very small growth rate of the $n = 1$ mode ($\gamma_{\text{SI}} \approx 2 \times 10^4 \text{ s}^{-1}$) suddenly changes at $t = 150 \mu\text{s}$ due to the non-linear interaction between the toroidal harmonics and becomes very large: $\gamma_{\text{SI}} \approx 4 \times 10^5 \text{ s}^{-1}$. In the non-linear phase of the mode, the $n = 1$ perturbation reaches

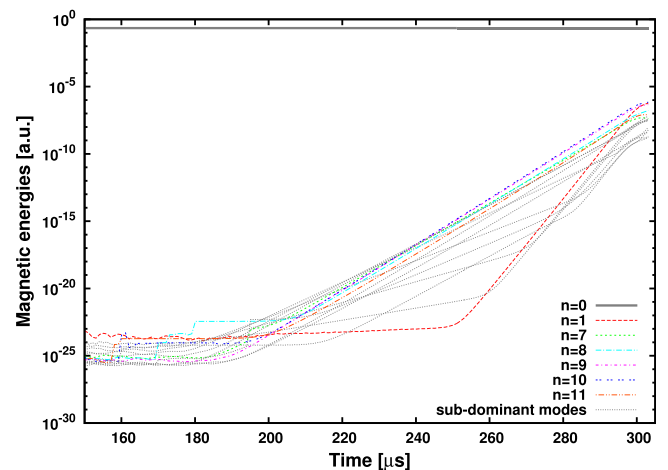


FIG. 5. Time-traces of the magnetic energies contained in the individual toroidal modes are shown for the simulation with periodicity 1. For clarity, kinetic energies are omitted and sub-dominant modes are only indicated by dotted gray lines. It is remarkable that the $n = 1$ mode reaches a comparable energy level at the onset of non-linear saturation as the $n = 10$ mode, which is the linearly most unstable mode.

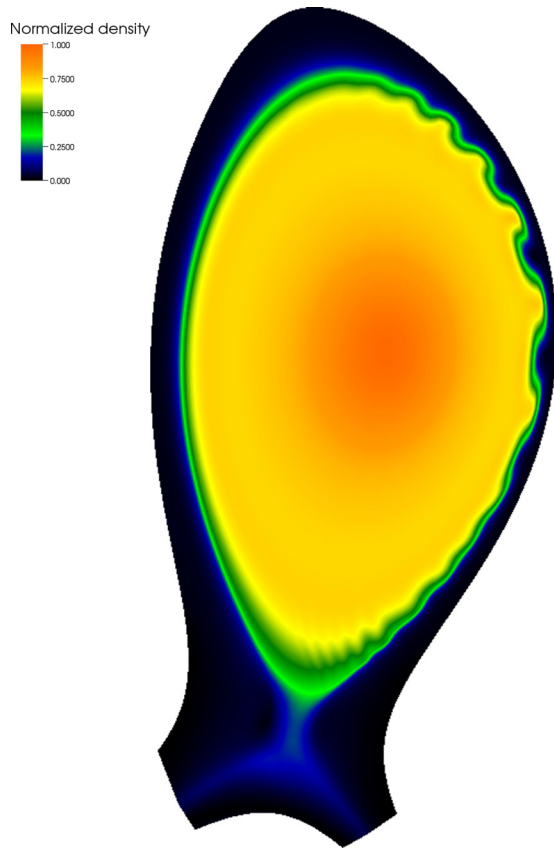


FIG. 6. The density-perturbation observed in the simulation with periodicity 1 is plotted at $294 \mu\text{s}$. The ballooning-structures become less regular and perturbations are strong only within a localized region. In the cross-section shown, this region is located on the upper low-field side.

a similar magnetic energy as the $n = 10$ perturbation which remains dominant also at the beginning of non-linear saturation ($t \approx 300 \mu\text{s}$). A first important effect that cannot be covered in simulations with low toroidal resolution (i.e., high periodicity) is that low- n modes can grow to large amplitudes non-linearly. The growth rate of the dominant mode

($n = 10$ in our case) is not affected significantly by the toroidal mode-coupling. Also, the radial propagation velocity of the filaments into the vacuum region hardly changes compared to the case with low toroidal resolution: The filaments accelerate in the beginning and saturate at a velocity of about 3 km/s .

The developing density perturbation is shown in Figure 6. Also with high toroidal resolution, a ballooning-like structure is produced at the low-field side of the plasma. The poloidal size of the ballooning-fingers is around $10\text{--}12 \text{ cm}$ at the midplane. In comparison to simulations with low toroidal resolution, these structures are a bit smaller. A significant difference becomes obvious when comparing Figures 4 and 6: Due to the mode-coupling, not all fingers grow to the same amplitude. A cluster of fingers can be seen that develops much stronger than the rest of the ballooning-structures. A strong localization of perturbations has also been observed in a ballooning-instability simulated with the BOUT code.²²

The localization of the perturbation becomes even more obvious when the magnetic footprint of the mode is considered. In Figure 7, the perturbation of the poloidal magnetic flux is plotted for simulations with different periodicities. Clearly, the localization of the mode can only be described correctly in simulations with periodicity 1. Figure 8 shows the perturbation of the poloidal flux at the outboard midplane versus the toroidal angle.

The perturbation is already localized in the linear phase of the mode. A qualitative change between the linear and the non-linear phases is shown in Figure 9, where the current perturbation is plotted for two different time-frames in the simulation with periodicity 1. In the non-linear phase where the ballooning-fingers become visible in the density perturbation, the previously alternating current filaments merge at the position of the separatrix around the outer midplane. Large areas with positive respectively negative currents are created.

The strongest perturbations of all physical quantities are localized in a flux-tube like region which extends from the

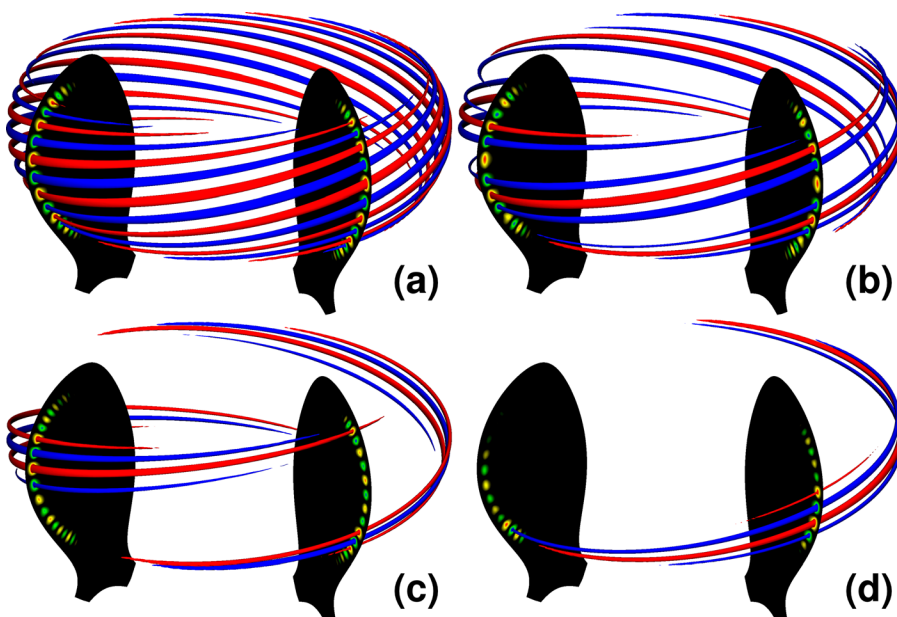


FIG. 7. Contours of the poloidal flux perturbation are shown for simulations with (a) periodicity 8, (b) 4, (c) 2, and (d) 1, respectively. The red and blue contours are plotted at the surfaces corresponding to the perturbed poloidal flux values $\tilde{\Psi}_{\text{red/blue}} = \pm 0.7 \cdot (|\tilde{\Psi}_{\text{min}}| + \tilde{\Psi}_{\text{max}})/2$. Here, $\tilde{\Psi}_{\text{min}}$ and $\tilde{\Psi}_{\text{max}}$ denote the strongest negative and positive perturbation values, respectively. At lower periodicities, the perturbation steadily gets more localized.

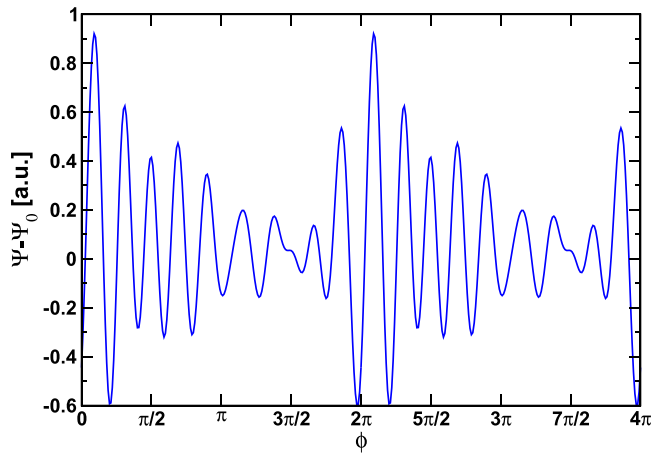


FIG. 8. The perturbation of the poloidal flux at the outboard midplane is shown for the simulation with periodicity 1 versus the toroidal angle for two transits around the torus. The perturbation amplitude shows a strong toroidal variation equivalent to a localization of the perturbation to $\Delta\phi \approx 3$ rad (FWHM). As equilibrium, boundary conditions, and sources are completely axis-symmetric, the localization position is essentially arbitrary which proves to be true when looking at a set of different simulations.

vicinity of the lower active X-point along magnetic field lines to the vicinity of the upper inactive X-point (compare Figure 7). The perturbations are strongest around the mid-plane. As an exception, v_{\parallel} is perturbed especially around the end-points of this flux-tube, a consequence of field-line stagnation close to the X-points. However, the radial perturbation positions differ as shown in Figure 10. It can be seen that the strongest perturbations of the magnetic quantities Ψ and j are located in the region of strong plasma current, while the kinetic quantities are perturbed further outwards in the region of strong pressure gradients.

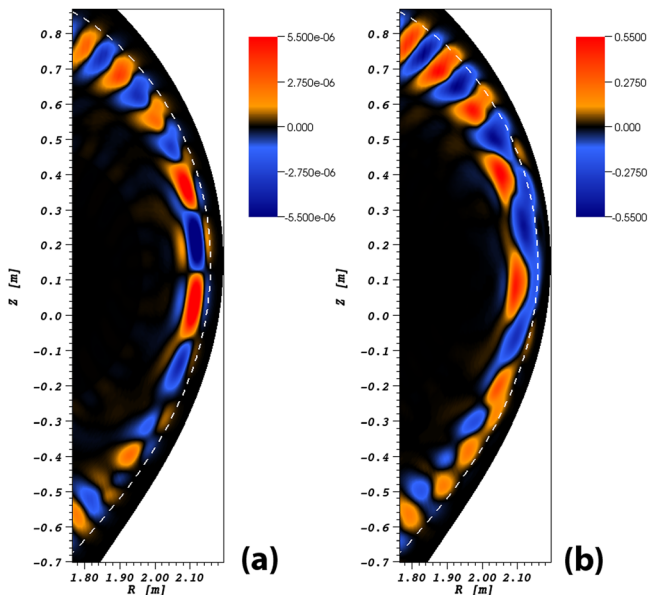


FIG. 9. The current perturbation at the plasma edge is shown for the simulation with periodicity 1 in the (a) linear ($240 \mu s$) and (b) non-linear phases ($300 \mu s$). In the non-linear phase, large regions with positive respectively negative current (this cross-section) form at the separatrix (dashed line) around the midplane.

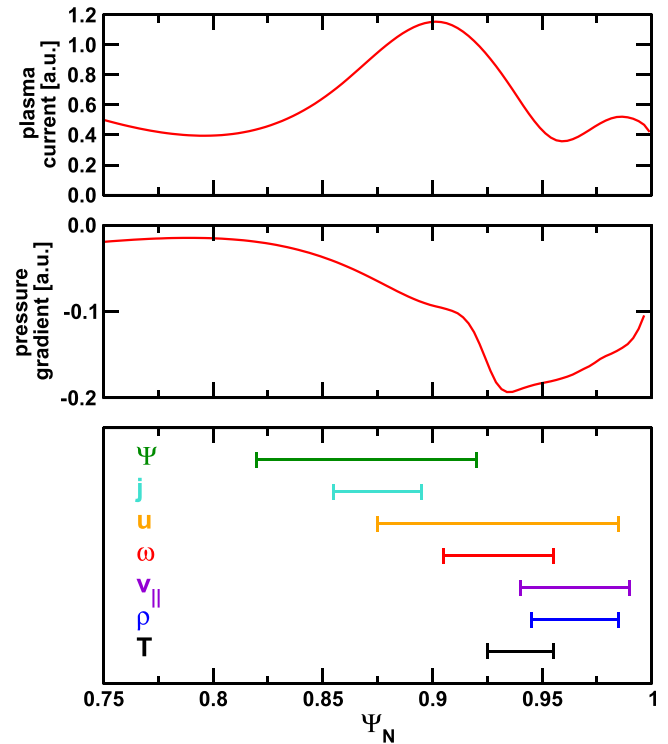


FIG. 10. For the simulation with periodicity 1, the radial positions of the strongest perturbations are shown at $t = 300 \mu s$ for the seven physical variables and are compared to profiles of the plasma current and the pressure gradient.

C. Towards more realistic resistivities

This section briefly shows results for simulations with the plasma viscosity and resistivity reduced by a factor of 10 (eta6 cases) compared to the simulations shown above. To be able to resolve these more realistic parameters, the number of 2D Bezier elements in the poloidal plane was increased by a factor of two. These simulations need to be considered with care as the most unstable mode is $n = 13$ while we do not take into account mode numbers beyond $n = 16$ for computational reasons.

It can be seen that a strong localization of the perturbations is observed at periodicity 1 as in the eta5-cases. This is shown for the perturbation of the poloidal flux in Figure 11. In contrast to the eta5-simulations, the perturbation maximum is not located around the midplane but more towards the top and bottom regions of the low-field side. This distribution of the flux-perturbation is not an artifact caused by cutting toroidally at $n = 16$: A simulation with periodicity 2 was carried out in which the toroidal modes $n = 0, 2, \dots, 20, 22$ are resolved, where the strongest perturbation of the poloidal flux is not observed at the midplane but above and below it as well.

At ASDEX Upgrade, an off-midplane mode-structure has recently been observed in the temperature using ECE-imaging.²³ In our simulations, the perturbation maximum of the kinetic quantities is, however, located around the mid-plane. This is a consequence of the comparably large plasma resistivities in our simulations which allow magnetic and kinetic quantities to decouple. At smaller resistivities, which

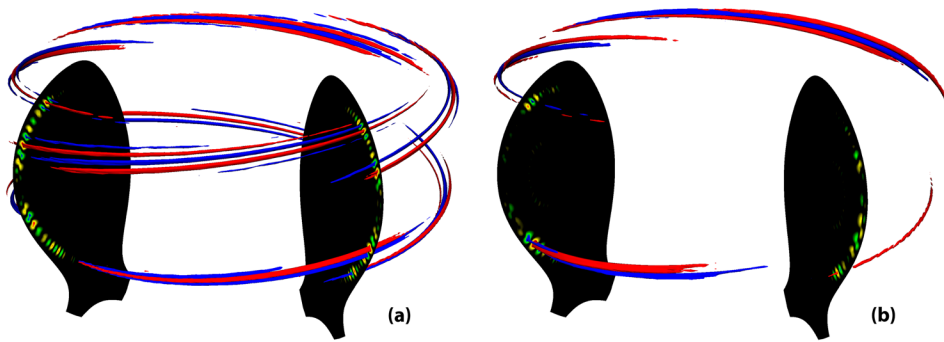


FIG. 11. For simulations with (a) periodicity 2 respectively (b) 1 where the plasma resistivity and viscosity is reduced by a factor of 10 compared to the simulations presented above, the poloidal flux perturbation is shown analogously to Figure 7. A strong localization of perturbations is observed in these simulations as well.

we cannot resolve at present, also the kinetic quantities might show an off-midplane behavior.

V. COMPARISON TO EXPERIMENTS

In this section, some properties of the simulated edge instabilities are compared to experimental observations. This shows that important aspects of the early phase of edge localized modes are well described by the reduced MHD model. More detailed comparisons between JOREK simulations of complete ELM crashes and experimental measurements at ASDEX Upgrade are planned for the future (e.g., evolution of pedestal gradients, detachment of filaments, heat-flux patterns at divertor plates).

The poloidal flux perturbation from the simulation with periodicity 1 shown in Figure 8 exhibits a toroidal localization: Large perturbation amplitudes are localized to a region of about $\Delta\phi \approx 3$ rad. Thus, the modes we observe in our simulations of the early ELM phase when simulating the full torus (periodicity 1) exhibit a similar magnetic structure as so-called solitary magnetic perturbations recently discovered at the ELM onset in ASDEX Upgrade and described in great detail in Ref. 24. From the systematic analysis of a large number of ELM crashes, a continuous distribution of the mode solitariness was reported between cases with a very pronounced toroidal localization (an example is shown in Figure 12) and cases with a magnetic perturbation strength that is toroidally virtually uniform. The toroidal localization observed in our simulations (localized to $\Delta\phi \approx 3$ rad) is less pronounced than the extreme example of Figure 12(b) with $\Delta\phi \approx 1.3$ rad. A direct comparison is planned for the future

making use of a virtual magnetic diagnostic which determines magnetic signals from the simulations at the same positions as the Mirnov coils. Toroidally asymmetric structures at ELMs are also described from experimental observations in Refs. 25–28. In analytical calculations, localized instabilities were also reported by Wilson *et al.*²⁹ These “explosive ballooning” instabilities grow much faster non-linearly than linearly, and a poloidal narrowing of the instability in the non-linear phase is reported. Both features are not observed in the simulated edge instabilities, which indicate that different mechanisms are responsible for the localization in our simulations.

The dominant toroidal mode turns out to be 10 in the simulations. With the plasma resistivity reduced towards more realistic values, the dominant mode number shifts towards 13. This is in quite good agreement to experimental findings in the tokamaks ASDEX Upgrade and MAST for type-I ELMs, where mode-numbers of 8–24 were observed in energy deposition patterns,²⁷ around 15 was found from measurements with the midplane manipulator and visible-light imaging,³⁰ and mode numbers of 18 ± 4 have been obtained for the onset of the ELM-crash using ECE-Imaging.²³ Uncertainties in our simulations come from the limited poloidal resolution and the neglect of diamagnetic stabilization as discussed in Sec. III.

Low- n modes gain large amounts of energy non-linearly in our simulations with periodicity 1. This allows them to interact much more efficiently with core-MHD modes like tearing modes which typically also feature low toroidal mode numbers like 1 or 2. Indeed, there is experimental evidence from the DIII-D tokamak that ELMs can be an

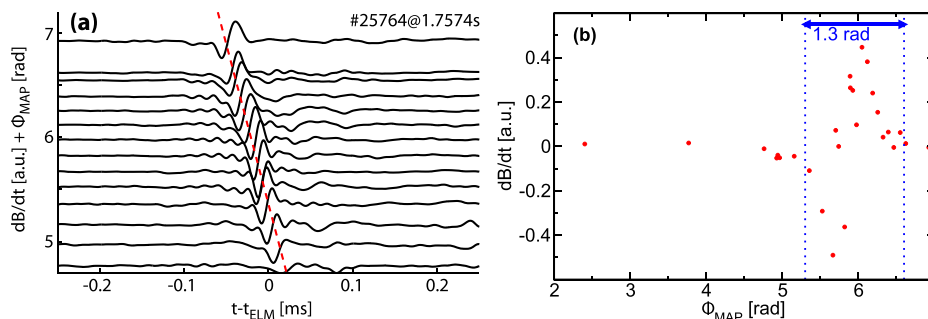


FIG. 12. (a) Magnetic signals from selected Mirnov-coils are shown for a strongly localized solitary magnetic perturbation in ASDEX Upgrade as in Ref. 24. All measurement locations are mapped to a common toroidal angle ϕ_{MAP} via field-line tracing. The magnetic perturbation propagates with constant toroidal velocity in the electron diamagnetic drift direction in the lab-frame as indicated by the red dashed line. The onset time of the erosion of pedestal temperature and density profiles is denoted t_{ELM} . (b) The time-derivative of the magnetic field measured by Mirnov coils is plotted versus the toroidal mapping angle ϕ_{MAP} at $t-t_{\text{ELM}} = -0.03$ ms. The solitary magnetic perturbation is localized to $\Delta\phi \approx 1.2$ rad.

important triggering mechanism for neoclassical tearing modes.³¹ The poloidal extent of filaments on the outer midplane observed in simulations with high toroidal resolution is around 10–12 cm. Measurements in ASDEX Upgrade and MAST revealed filament sizes perpendicular to the field lines of 5–10 cm.³⁰ For ASDEX Upgrade, perpendicular and poloidal filament sizes are equivalent due to the small field-line pitch-angle such that simulation results and experimental observations show good agreement here as well.

In the simulations, the radial velocity of the developing finger structures saturates at about 3 km/s after an initial acceleration. This corresponds to a distribution of the radial filament speed with an upper limit of 3 km/s. This velocity depends on the stability of the initial equilibrium. The unrealistically large values for the plasma resistivity might lead to an over-estimation of the filament speeds, while the ideal-wall boundary conditions tend to reduce the radial velocity. In experimental measurements, the radial filament speed is found to be distributed around 1 km/s in ASDEX Upgrade.^{32,33} Filament speeds faster than 2 km/s occur in 20% of the cases in both references, and almost no filaments faster than 3 km/s are observed. Hence, radial filament speeds in simulations and experimental measurements seem to agree reasonably well.

In the magnetic quantities, an off-midplane mode-structure is observed in the simulations with lower plasma resistivity (eta6 simulations). As the resistivity is still unrealistically large in these simulations, magnetic and kinetic quantities are decoupled such that the strongest perturbation of the temperature is located at the midplane. Still, this might be related to the off-midplane structures observed by ECE-imaging in ASDEX Upgrade.²³

VI. CONCLUSIONS AND OUTLOOK

Exponentially growing ballooning-like modes have been simulated with the reduced-MHD version of the non-linear MHD code JOREK in the geometry and using the profiles of a typical ASDEX Upgrade H-mode discharge. Dominant toroidal mode numbers, poloidal filament sizes, and radial filament-propagation speeds of these instabilities are in good agreement with experimental observations for type-I ELMs in ASDEX Upgrade. At sufficient toroidal resolution, perturbations show a pronounced toroidal and poloidal localization which is compatible with solitary magnetic perturbations recently discovered in ASDEX Upgrade. In some cases, the perturbation of the magnetic flux is stronger at the top and bottom low-field side than at the midplane. Presumably due to a decoupling of magnetic and kinetic quantities caused by the unrealistically large plasma resistivity, density, and temperature perturbations are always localized on the midplane of the low-field side. Strong perturbations in the low- n modes are triggered non-linearly in the simulations with periodicity 1 and might explain the strong interaction of ELMs with core-MHD modes like neoclassical tearing modes observed in some experiments.

While this work concentrates on the early phase of an ELM, further studies are planned to compare the simulation of a full ELM crash to experimental observations requiring a

more sophisticated modeling of the scrape-off layer. Simulations of a full ELM cycle will also be attempted. Future numerical improvements and increased computational resources will be used to advance our investigations towards more realistic plasma parameters while keeping high toroidal resolutions.

ACKNOWLEDGMENTS

The simulations were mostly carried out on the HPC-FF computing cluster in Jülich, Germany. K.L. would like to acknowledge the support by the Austrian Science Fund (FWF) under Grant No. P19901. Additionally, the authors would like to thank Erika Strumberger and Mike Dunne for their help with the plasma equilibrium reconstruction and Klaus Reuter for assistance with visualizations.

APPENDIX: A DERIVATION OF THE INDUCTION EQUATION

The reduced MHD equations implemented in the JOREK code can be derived following Ref. 16. For the induction equation, this is shown in the following. The starting points are the well-known expression for the electric field in the MHD approximation

$$\mathbf{E} = -\mathbf{v} \times \mathbf{B} + \eta \mathbf{j}, \quad (\text{A1})$$

and the Maxwell-Faraday law expressed in the vector potential \mathbf{A}

$$\frac{\partial \mathbf{A}}{\partial t} = -\mathbf{E} - F_0 \nabla u. \quad (\text{A2})$$

Inserting Eqs. (A1) into (A2) and multiplying it with the toroidal unity vector $\hat{\mathbf{e}}_\phi$ yields

$$\frac{\partial \Psi}{\partial t} = \eta j + (\mathbf{v} \times \mathbf{B}) \cdot \hat{\mathbf{e}}_\phi - F_0 \nabla u \cdot \hat{\mathbf{e}}_\phi, \quad (\text{A3})$$

where the poloidal flux is identified as the major radius times the toroidal component of the vector potential, $\Psi \equiv R \mathbf{A} \cdot \hat{\mathbf{e}}_\phi$, and $j = -\mathbf{j} \cdot \hat{\mathbf{e}}_\phi$ denotes the toroidal plasma current. Using Eqs. (8) and (9), this can be written as

$$\frac{\partial \Psi}{\partial t} = \eta j - R[u, \Psi] - F_0 \frac{\partial u}{\partial \phi}, \quad (\text{A4})$$

which is the induction equation (Eq. (3)) solved in the JOREK reduced MHD model with the Poisson bracket $[u, \Psi] = \frac{\partial u}{\partial R} \frac{\partial \Psi}{\partial Z} - \frac{\partial u}{\partial Z} \frac{\partial \Psi}{\partial R}$. In the last step, the reduced MHD approximation to first order in $\varepsilon = \nabla_{\parallel} \Psi / \nabla_{\perp} \Psi \ll 1$ yielding $\mathbf{v}_{\text{pol}} \approx \mathbf{v}_{\perp}$ was applied.

The poloidal components of Eq. (A2), obtained by applying the operator $\hat{\mathbf{e}}_\phi \times$ to this equation, yield a definition equation for the poloidal velocity (see poloidal components of Eq. (8)), in which u can be identified as the poloidal velocity stream function. In this set of equations, u also acts as electric potential (except for a constant factor F_0).

Galilei-invariance of the induction equation (Eq. (A2)) is not obvious at first glance. However, the proof is straightforward when taking into account that the scalar potential

$\phi = F_0 u$ is modified according to $\phi \rightarrow \phi - \mathbf{v}_0 \cdot \mathbf{A}$ under the transformation $\mathbf{v} \rightarrow \mathbf{v} - \mathbf{v}_0$ while the vector potential remains unchanged (non-relativistic limit). In the large aspect-ratio limit, it can also be shown easily that the reduced-MHD induction equation (Eq. (A4)) is invariant to a transformation $\mathbf{v} \rightarrow \mathbf{v} - \mathbf{v}_z$ with z along the cylinder axis, as the scalar potential transforms according to $\phi \rightarrow \phi - v_z \Psi$.

- ¹A. Loarte, G. Saibene, R. Sartori, D. Campbell, M. Becoulet, L. Horton, T. Eich, A. Herrmann, G. Matthews, N. Asakura, A. Chankin, A. Leonard, G. Porter, G. Federici, G. Janeschitz, M. Shimada, and M. Sugihara, "Characteristics of type I ELM energy and particle losses in existing devices and their extrapolation to ITER," *Plasma Phys. Controlled Fusion* **45**(9), 1549 (2003).
- ²N. Klimov, V. Podkovyrov, A. Zhitlukhin, D. Kovalenko, J. Linke, G. Pintsuk, I. Landman, S. Pestchanyi, B. Bazylev, G. Janeschitz, A. Loarte, M. Merola, T. Hirai, G. Federici, B. Riccardi, I. Mazul, R. Giniyatulin, L. Khimchenko, and V. Koidan, "Experimental study of PFCs erosion and eroded material deposition under ITER-like transient loads at the plasma gun facility QSPA-T," *J. Nucl. Mater.* **415**(1, Suppl.), S59–S64 (2011).
- ³G. T. A. Huysmans and O. Czarny, "MHD stability in X-point geometry: Simulation of ELMs," *Nuclear Fusion* **47**(7), 659 (2007).
- ⁴G. T. A. Huysmans, R. Abgrall, M. Becoulet, R. Huart, B. Nkonga, S. Pamela, E. van der Plas, and P. Ramet, "Non-linear MHD simulations of ELMs," in Proceedings of the 35th EPS Conference on Plasma Physics, Hersonissos, Greece, 9–13 June 2008, P–2.065.
- ⁵G. T. A. Huysmans, S. Pamela, E. van der Plas, and P. Ramet, "Non-linear MHD simulations of edge localized modes (ELMs)," *Plasma Phys. Controlled Fusion* **51**(12), 124012 (2009).
- ⁶S. Pamela, G. Huysmans, and S. Benkadda, "Influence of poloidal equilibrium rotation in MHD simulations of edge-localized modes," *Plasma Phys. Controlled Fusion* **52**(7), 075006 (2010).
- ⁷G. Huysmans, S. Pamela, M. Beurskens, M. Becoulet, and E. van der Plas, "Non-linear MHD simulation of natural and pellet triggered ELMs," in Proceedings of the 23rd IAEA Fusion Energy Conference, Daejeon, South Korea, 11–16 October 2010.
- ⁸S. J. P. Pamela, G. T. A. Huysmans, M. N. A. Beurskens, S. Devaux, T. Eich, S. Benkadda, and JET EFDA Contributors, "Nonlinear MHD simulations of edge-localized-modes in JET," *Plasma Phys. Controlled Fusion* **53**(5), 054014 (2011).
- ⁹M. Hölzl, S. Günter, and ASDEX Upgrade Team, "Reduced-MHD simulations of edge localized modes in ASDEX Upgrade (P2.078)," in Proceedings of the 38th EPS Conference on Plasma Physics, Strasbourg, France, 2011.
- ¹⁰B. D. Dudson, X. Q. Xu, M. V. Umansky, H. R. Wilson, and P. B. Snyder, "Simulation of edge localized modes using BOUT++," *Plasma Phys. Controlled Fusion* **53**(5), 054005 (2011).
- ¹¹A. Y. Pankin, G. Bateman, D. P. Brennan, A. H. Kritiz, S. Kruger, P. B. Snyder, C. Sovinec, and NIMROD Team, "Modelling of ELM dynamics for DIII-D and ITER," *Plasma Phys. Controlled Fusion* **49**(7), S63 (2007).
- ¹²L. E. Sugiyama and H. R. Strauss, "Magnetic X-points, edge localized modes, and stochasticity," *Physics of Plasmas* **17**(6), 062505 (2010).
- ¹³O. Czarny and G. Huysmans, "Bezier surfaces and finite elements for MHD simulations," *J. Comput. Phys.* **227**(16), 7423–7445 (2008).
- ¹⁴A. Herrmann, "Special issue: ASDEX Upgrade," *Fusion Sci. Technol.* **44**(3), 569–742 (2003).
- ¹⁵E. Wolfrum, M. Bernert, J. E. Boom, A. Burckhart, I. G. J. Classen, G. D. Conway, T. Eich, R. Fischer, A. Gude, A. Herrmann, N. C. Luhmann, Jr., M. Maraschek, R. McDermott, H. K. Park, T. Puetterich, J. Vicente, B. Wieland, M. Willensdorfer, and ASDEX Upgrade Team, "Characterization of edge profiles and fluctuations in discharges with type-II and nitrogen-mitigated edge localized modes in ASDEX Upgrade," *Plasma Phys. Controlled Fusion* **53**(8), 085026 (2011).
- ¹⁶H. R. Strauss, "Reduced MHD in nearly potential magnetic fields," *J. Plasma Phys.* **57**(1), 83–87 (1997).
- ¹⁷P. C. Stangeby and A. V. Chankin, "The ion velocity (Bohm–Chodura) boundary condition at the entrance to the magnetic presheath in the presence of diamagnetic and $\mathbf{E} \times \mathbf{B}$ drifts in the scrape-off layer," *Phys. Plasmas* **2**(3), 707–715 (1995).
- ¹⁸C. Hirsch, *Numerical Computation of Internal and External Flows, Volume 1, Fundamentals of Numerical Discretization* (Wiley, 1989).
- ¹⁹See <http://www.gforge.inria.fr/projects/pastix/> for the website of PASTIX.
- ²⁰P. J. McCarthy, P. Martin, and W. Schneider, "The CLISTE interpretive equilibrium code," Technical Report IPP-Report 5/85, Max-Planck-Institut für Plasmaphysik, Boltzmannstraße 2, 85748 Garching, Germany, 1999.
- ²¹P. J. McCarthy, "Analytical solutions to the Grad-Shafranov equation for tokamak equilibrium with dissimilar source functions," *Phys. Plasmas* **6**(9), 3554 (1999).
- ²²P. B. Snyder, H. R. Wilson, and X. Q. Xu, "Progress in the peeling-ballooning model of edge localized modes: Numerical studies of nonlinear dynamics," *Phys. Plasmas* **12**(5), 056115 (2005).
- ²³J. E. Boom, I. G. J. Classen, P. C. de Vries, T. Eich, E. Wolfrum, W. Suttrop, R. P. Wenninger, A. J. H. Donn, B. J. Tobias, C. W. Domier, N. C. Luhmann, Jr., H. K. Park, and ASDEX Upgrade Team, "2D ECE measurements of type-I edge localized modes at ASDEX Upgrade," *Nucl. Fusion* **51**(10), 103039 (2011).
- ²⁴R. P. Wenninger, H. Zohm, J. Boom, T. Eich, M. Garcia-Munoz, M. Hoelzl, T. Lunt, M. Maraschek, H. W. Mueller, F. Sommer, E. Viezzer, and ASDEX Upgrade Team, "Solitary magnetic perturbations at the ELM onset," *Nucl. Fusion* (accepted).
- ²⁵H. Reimerdes, A. Pocheleon, and W. Suttrop, "Toroidally asymmetric ELM precursors in TCV," *Nucl. Fusion* **38**(3), 319 (1998).
- ²⁶M. Bécoulet, G. Huysmans, Y. Sarazin, X. Garbet, Ph. Ghendrih, F. Rimini, E. Joffrin, X. Litaudon, P. Monier-Garbet, J.-M. Ané, P. Thomas, A. Grosman, V. Parail, H. Wilson, P. Lomas, P. deVries, K.-D. Zastrow, G. F. Matthews, J. Lonroth, S. Gerasimov, S. Sharapov, M. Gryaznevich, G. Counsell, A. Kirk, M. Valovic, R. Buttery, A. Loarte, G. Saibene, R. Sartori, A. Leonard, P. Snyder, L. L. Lao, P. Gohil, T. E. Evans, R. A. Moyer, Y. Kamada, A. Chankin, N. Oyama, T. Hatae, N. Asakura, O. Tudisco, E. Giovannozzi, F. Crisanti, C. P. Perez, H. R. Koslowski, T. Eich, A. Sips, L. Horton, A. Herrmann, P. Lang, J. Stober, W. Suttrop, P. Beyer, S. Saarelma, and Contributors to JET-EFDA Workprogramme, "Edge localized mode physics and operational aspects in tokamaks," *Plasma Phys. Controlled Fusion* **45**(12A), A93 (2003).
- ²⁷T. Eich, A. Herrmann, and J. Neuhauser, "Nonaxisymmetric energy deposition pattern on ASDEX Upgrade divertor target plates during type-I edge-localized modes," *Phys. Rev. Lett.* **91**, 195003 (2003).
- ²⁸V. V. Bobkov, M. Becoulet, T. Blackman, J. Brzozowski, C. Challis, S. Gerasimov, P. U. Lamalle, M. Maraschek, M.-L. Mayoral, I. Monakhov, J.-M. Noterdaeme, G. Saibene, A. Walden, P. Wouters, ASDEX Upgrade Team, and JET-EFDA Contributors, "Studies of ELM toroidal asymmetry using ICRF antennas at JET and ASDEX Upgrade," in Proceedings of the 31st EPS Conference on Plasma Physics, London, UK, 28 June–2 July 2004.
- ²⁹H. R. Wilson and S. C. Cowley, "Theory for explosive ideal magnetohydrodynamic instabilities in plasmas," *Phys. Rev. Lett.* **92**, 175006 (2004).
- ³⁰A. Kirk, T. Eich, A. Herrmann, H. W. Muller, L. D. Horton, G. F. Counsell, M. Price, V. Rohde, V. Bobkov, B. Kurzan, J. Neuhauser, H. Wilson, ASDEX Upgrade, and MAST Teams, "The spatial structure of type-I ELMs at the mid-plane in ASDEX Upgrade and a comparison with data from MAST," *Plasma Phys. Controlled Fusion* **47**(7), 995 (2005).
- ³¹O. Sauter, R. J. La Haye, Z. Chang, D. A. Gates, Y. Kamada, H. Zohm, A. Bondeson, D. Boucher, J. D. Callen, M. S. Chu, T. A. Gianakon, O. Gruber, R. W. Harvey, C. C. Hegna, L. L. Lao, D. A. Monticello, F. Perkins, A. Pletzer, A. H. Reiman, M. Rosenbluth, E. J. Strait, T. S. Taylor, A. D. Turnbull, F. Waelbroeck, J. C. Wesley, H. R. Wilson, and R. Yoshino, "Beta limits in long-pulse tokamak discharges," *Phys. Plasmas* **4**(5), 1654–1664 (1997).
- ³²A. Schmid, A. Herrmann, H. W. Miller, and ASDEX Upgrade Team, "Experimental observation of the radial propagation of ELM induced filaments on ASDEX Upgrade," *Plasma Phys. Controlled Fusion* **50**(4), 045007 (2008).
- ³³A. Kirk, H. W. Muller, A. Herrmann, M. Kocan, V. Rohde, P. Tamain, and ASDEX Upgrade Team, "Parameters determining the radial propagation of type-I edge localized modes (ELMs) in ASDEX Upgrade," *Plasma Phys. Controlled Fusion* **53**(3), 035003 (2011).